Article

Not peer-reviewed version

Synthesis, Structural, Optical, and Electrical Characterization of Bio-Chitosan/$Na_{0.5}Bi_{0.5}TiO_3$ Composite Thin Films Materials

Jacem Zidani , Khaoula Hassine , Moneim Zannen , Andreas Zeinert , Antonio Da Costa , Anthony FERRI , Jamal Belhadi , Mustapha Majdoub , Mimoun El Marssi , Abdelilah LAHMAR *

Posted Date: 12 September 2023

doi: 10.20944/preprints202309.0687.v1

Keywords: composite films; chitosan; NBT; dielectric properties; local piezoelectric response; optical properties

Article

Synthesis, Structural, Optical, and Electrical Characterization of Bio-Chitosan/$Na_{0.5}Bi_{0.5}TiO_3$ Composite Thin Films Materials

Jacem Zidani [1,2], Khaoula Hassine [2], Moneim Zannen [2], Andreas Zeinert [1], Antonio Da Costa [3], Anthony Ferri [3], Jamal Belhadi [1], Mustapha Majdoub [2], Mimoun El Marssi [1] and Abdelilah Lahmar [1]*

[1] Laboratoire de Physique de la Matière Condensée (LPMC), Université de Picardie Jules Verne, 33 rue Saint-Leu, 80039 Amiens Cedex 1, France
[2] Laboratory of Interfaces and Advanced Materials (LIMA), Faculty of Sciences of Monastir, University of Monastir, Bd. Of the Environment, Monastir 5019, Tunisia.
[3] University of Artois, CNRS, Centrale Lille, University of Lille, UMR 8181 – UCCS – Unité de Catalyse et Chimie du Solide, Lens, France
* Correspondence: abdel.ilah.lahmar@u-picardie.fr; Tel.: +33-3-22-82-76-91

Abstract: The purpose of this research work was to synthesis bio-derived nanocomposite films by incorporating $Na_{0.5}Bi_{0.5}TiO_3$ (NBT) nanoparticles into Chitosan matrix. The NBT nanoparticles were synthesized using a traditional solid-state technique. Then, through a solution casting approach, flexible composite films were fabricated using Chitosan polymer. The morphology and structural assessments were carried out utilizing scanning electron microscopy (SEM), X-ray diffraction and fourier transform infrared technique. The SEM micrographs showed that NBT nanoparticles were randomly distributed and interconnected with other particles, forming interconnected grains with substantial interspaces within the matrix. The spectral response between 300 and 800 nm of the composites is mainly governed by light scattering of NBT particles with diameter sizes in the 100 - 400 nm range and the bandgap of the NBT phase. The dielectric studies demonstrated that the composite films exhibited higher dielectric values compared to the pure Chitosan film. Besides, the increase of NBT amount was found to increase the dielectric values. Additionally, local piezoelectric measurements reveal the expected piezoelectric and ferroelectric behavior for the NBT particles dispersed into the polymer matrix, as locally probed by Piezoresponse Force Microscopy. The studied system bears interest for advanced biocompatible opto- and piezo-electric materials.

Keywords: composite films; chitosan; NBT; dielectric properties; local piezoelectric response; optical properties

1. Introduction

Harnessing the abundant mechanical energy generated by vibrations, such as those caused by human movement, transport, and sound waves has become one of the concerns of both industrial and scientific communities to ensure the ecological transition and satisfy a new technological demand respecting the human health and the environment [1]. This renewable and secure energy source has the potential to greatly impact our daily lives. It would enable numerous health monitoring devices, safety equipment, sensors, alarms, lights, and other compact devices to operate autonomously, reducing our reliance on external power sources like the electricity grid and batteries [2]. As a result, our overall energy consumption would be significantly reduced. Piezoelectric generators offer substantial potential for powering portable devices and self-sustaining electronic systems by extracting mechanical energy. The piezoelectric mechanism's advantages over other conversion methods lie in its high energy density and scalability across a broad range of sizes.

 doi:10.20944/preprints202309.0687.v1

Piezoelectric materials, renowned for their ability to convert mechanical energy into electrical signals, are considered smart materials due to their reversible nature [3]. The manifestation of this phenomenon relies heavily on the crystal lattice structure of the materials employed and the existence of a center of symmetry within their structure [3]. Poly (vinylidene fluoride) (PVDF) is widely recognized as the most prominent piezoelectric polymer employed in numerous biomedical applications, primarily attributable to its elevated piezoelectric coefficient [4]. The PVDF, a polymer characterized by its crystalline structure, demonstrates remarkable piezoelectric properties [4]. While PVDF possesses a higher piezoelectric coefficient compared to other polymers, it falls short when compared to piezoceramics, which typically have a d_{33} value ranging from 13 to 28 pC/N [5]. However, PVDF is characterized by inadequate adhesion to other materials, limited thermal stability, and the inability to generate uniform films [4].

Currently, the majority of commercially available piezoelectric generators are based on lead-containing materials. Particularly, those relying on lead-zirconate titanate (PZT) have demonstrated superior piezoelectric performance in numerous applications [6–8]. However, the utilization of lead-based materials presents significant challenges regarding environmental compatibility. Consequently, there is a pressing requirement to develop lead-free alternatives that can exhibit comparable piezoelectric properties to those achieved with lead-containing materials [9].

Lately, there has been a growing attention in utilizing biomaterials as alternatives to synthetize piezoelectric materials. Biomaterials offer superior biocompatibility, bioactivity, biodegradability, low immunogenicity, antimicrobial properties, and flexibility [3,10,11]. As a result, the scope of piezoelectric applications can be extended to the development of self-powered wearable electronic devices. Extensive research has been conducted on the piezoelectric properties of bio-based materials originating from natural polymers like cellulose, chitin, and chitosan. Chitosan, an organic polymer, is an unbranched polysaccharide composed of β-1,4-D-glucosamine, obtained through the deacetylation process of chitin [12]. Chitin is present in the exoskeletons of crustaceans and the cellular walls of mushrooms and fungi [13,14]. Incorporating biopolymers into piezoelectric applications empowers polymers to operate effectively in wearable and pliable smart devices. Nonetheless, research pertaining to the utilization of chitosan in piezoelectric applications remains relatively constrained. Some studies have explored the piezoelectric properties of commercial chitosan, and findings indicate that its piezoelectricity is comparable to that of PVDF [15,16].

Nanocellulose and chitosan have gained attention for their potential applications in various fields, including biodegradable energy harvesters and sensors. One key characteristic that makes these materials promising is their piezoelectricity, which enables them to generate electrical charges under mechanical stress [17]. Especially, as smart devices continue to proliferate within the Internet of Things (IoT), concerns have arisen regarding the environmental impact associated with waste and emissions [18]. Using biodegradable piezoelectric membranes to generate energy locally, offers a sustainable and economically viable solution for powering the IoT, in contrast to non-degradable materials or batteries. This approach aligns with the goal of minimizing environmental impact while maintaining efficient device functionality.

In this current study, we report on the synthesis of bio-derived and flexible nanocomposite films by incorporating $Na_{0.5}Bi_{0.5}TiO_3$ (NBT) nanoparticles into Chitosan polymer matrix using a solution casting approach. The structural, microstructural, optical, dielectric and piezoelectric properties of these films with different NBT content Ranging from 2 to 10% were investigated.

2. Materials and Methods

2.1. Preparation of NBT powder

The traditional solid-state process was used to prepare the $Na_{0.5}Bi_{0.5}TiO_3$ (NBT) powders. High purity precursors including Na_2CO_3 (99%), Bi_2O_3 (99%), TiO_2 (99.9%) were employed. The powder was measured, combined in accordance with the stoichiometric ratio, and thoroughly ground with ethanol in an agate mortar. The calcination was completed using a heating rate of 300°C/h for 3 hours at 900°C. The powders were then re-ground in an agate mortar to get the final NBT powder.

 doi:10.20944/preprints202309.0687.v1

2.2. Preparation of Chitosan polymer

The exoskeleton of the pink shrimp, scientifically known as "P. longirostris," was utilized in the production of chitosan. It came from a Tunisian processing factory.

To eliminate organics, proteins, and other contaminants, shells were recovered from shrimp feces and cleaned under running water. The tissue was then removed from the shells by boiling them in water for 0.5 hours, and then they were dried for 2 hours at 100°C to destroy the chitin's crystal structure [19]. In the end, a blender equipped with a sieve with a 0.1 mm diameter was used to break the dry shells. The obtained raw material is sealed in bags and kept in a freezer at 4°C.

2.2.1. Demineralization

To avoid chitin's hydrolysis, only diluted hydrochloric acid was employed to dissolve the calcium carbonate in the shells [20]. With steady stirring, the powder was demineralized with 2M HCl (1/10, w/v) at 60°C for 150 minutes. The decalcified shells underwent filtering and neutral pH washing with distilled water.

2.2.2. Deproteinization

Dried shells were demineralized under the same experimental conditions. With stirring, the dehydrated shells were deproteinized in 3 M of sodium hydroxide (NaOH) (1/10, w/v) at 80°C for 120 minutes. The material was filtered, cleaned, and dried at the end of this procedure, as before mentioned in the demineralization method.

2.2.3. Decolouration

"P. longirostris" crustacean chitin was slightly pink in color. The pigment traces that give this hue its existence is eliminated using a light oxidizing procedure [H_2O_2(0.1 M), HCl (10 mM) in a volume ratio of [9:1] and acetone (1:5 w/v) for 10 minutes. The material is then rinsed and dried for two hours at room temperature [21].

2.2.4. Deacetylation

Via the method proposed by Galed et al. [22], deacetylation was required for the process of conversion of chitin to chitosan (CS). With continual stirring at 110°C and 15 M NaOH (1/20, w/v), chitin was deacetylated. Following five hours, the sample is put under the hood and allowed to cool for 30 minutes at ambient temperature. Chitosan is subsequently rinsed with distilled water until the filtrate reaches a pH of 7, then dried at 60°C for twenty-four hours.

2.3. Preparation of films

To prepare the films, the required quantity of (3wt%) chitosan polymer was dissolved in (1wt%) acetic acid for 3 hours at room temperature.

Then, while continuously stirring, (2wt %) of glycerol was added to the solution. Following that, NBT powder was combined with the polymer solution using a magnetic stirrer for three hours in various mass ratios of 2%, 4%, 6%, 8%, and 10%, as shown in Figure 1.

The hybrid nanocomposite's preparation resembled other procedures that have been employed in the past somewhat [20,23]. The solution was produced and placed in a plastic petri dish which was placed in the oven for drying for 12 hours at 40°C.

2.4. Characterizations

The NBT powder and CS/NBT composite films were analyzed using a Bruker Discover Advance D8 diffractometer with CuKα = 1.5406 Å for XRD analysis. The morphology of the composites was observed using an FEI Quanta 200 FEG Environmental SEM. Infrared spectroscopy measurements of the composites were performed using a FTIR spectrometer IS50 ATR, collecting spectra within the range of 4000–400 cm^{-1}. Raman spectroscopy was carried out by a Renishaw micro-Raman

Preprints (www.preprints.org) | NOT PEER-REVIEWED | Posted: 12 September 2023 doi:10.20944/preprints202309.0687.v1

spectrometer, with a green laser excitation wavelength of 514.5 nm. The optical properties of the prepared systems were investigated using a V-670 UV–VIS spectrophotometer in the wavelength range of 200–800 nm at ambient temperature. As in these samples scattering of light occurs the reflectance and transmittance were captured by an integrating sphere. Thus, the specular and scattered light component was captured at the same time. Dielectric investigations were conducted at room temperature using a Solartron Impedance analyzer SI-12060 over a frequency range of 100 Hz to 1 MHz. The surface morphology of the CS/NBT10% composite was examined at the local scale using the AFM technique in alternative contact mode, also known as Tapping™ mode (TM-AFM). Then, to investigate the piezoelectric and ferroelectric properties, the dual AC resonance tracking (DART) method [24] from the PFM technique was employed under environmental conditions by using a commercial MFP-3D microscope (Asylum Research/Oxford Instruments, USA). For these measurements, Pt-coated silicon tip and calibrated cantilever with a stiffness of 2.34 $N.m^{-1}$ (PPP-EFM, Nanosensors) were utilized as the conductive probe. For PFM imaging, an AC driving voltage of 4 V was applied to the AFM tip. This allowed for the visualization and analysis of as-grown domain patterns of the sample under investigation. Additionally, PFM in spectroscopic mode was employed to record local piezoelectric hysteresis loops at the free surface (without top electrode) of the composites, giving access to the switching behavior and electromechanical activity of the probed domain beneath the tip. Such spectroscopic PFM analyses were performed by applying a continuous AC voltage (4 V) superimposed to an intermittent DC bias voltage, by selecting the remnant mode (i.e. at zero bias) in order to minimalize electrostatic contribution while promoting electromechanical response [25].

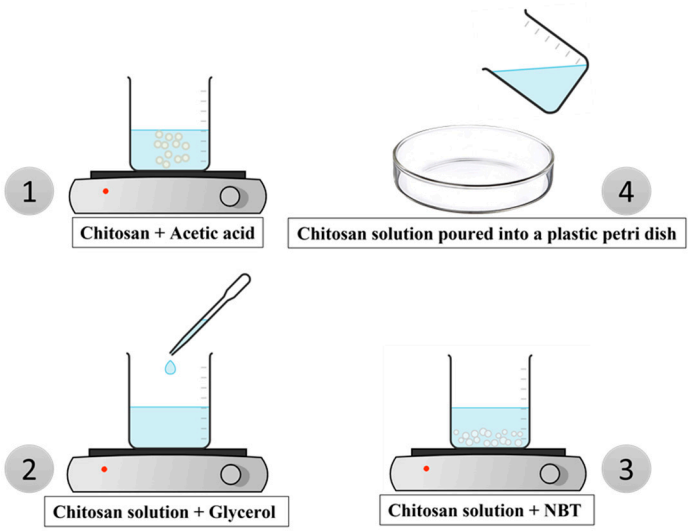

Figure 1. Schematic representation of synthesis chitosan + NBT membrane.

3. Results and discussion

3.1. Structural investigations

Figure 2 illustrates the results of the X-ray diffraction patterns of the NBT, CS, and CS/nano-NBT composite membranes.

The NBT powder exhibits a single perovskite phase without heterogeneous peaks, as can be shown in Figure 2. In the rhombohedral phase, the NBT powder is indexed with the space group R3c [26]. The Debye-Scherrer equation was used to determine the NBT crystallite size from the FWHM of the peaks which came out to 11.9 nm (1) [27]:

$$D = {}^{k\lambda}/_{\beta \cos\theta}$$

Preprints (www.preprints.org) | NOT PEER-REVIEWED | Posted: 12 September 2023 doi:10.20944/preprints202309.0687.v1

with D: the average crystallite size, k = 0.9: Scherrer's constant, λ (CuKα) = 1.5406 Å: the wavelength of the radiation used, β: the peak width at half maximum (FWHM) and θ: the Bragg angle of the most intense peak.

At 2θ = 19.6, the characteristic CS membrane peak could be seen which can be associated to the semicrystalline nature of the chitosan [28]. According to Pawlak et al. [29], Chitosan's semi crystallinity results from the compact arrangement of polymer molecules and the presence of potent intermolecular hydrogen bonding.

Other diffraction peaks appeared with the increase in the amount of NBT added at 22.44º, 32.16º, 39.80º, 46.39º and 57.81º of CS/nano-NBT composite membranes. These diffraction peaks were assigned to the (101), (110), (021), (202) and (122) planes of rhombohedral NBT [30]. The XRD spectra of composite films revealed an increase of the intensity of the principal peaks with increasing the quantity of NBT nanoparticles. The variations in intensities are caused by variations in the amounts of NBT nanoparticles contained [31]. Hence, XRD results underline the good dispersion of NBT nanoparticles on the Chitosan matrix.

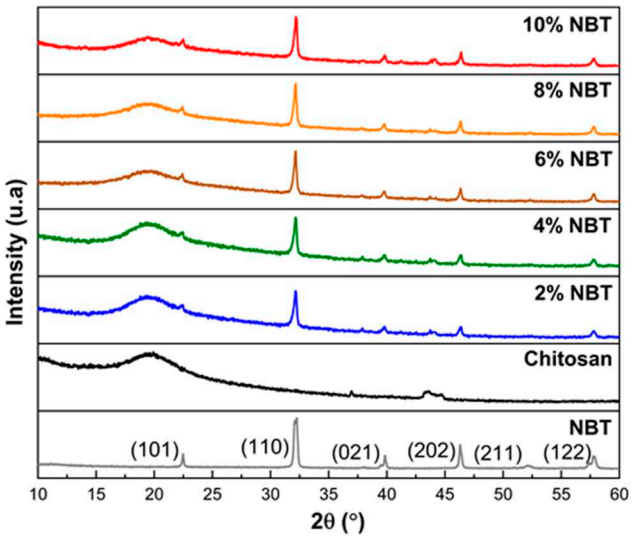

Figure 2. XRD of nanocomposite chitosan/NBT.

3.2. Vibrational investigations

The infrared spectra of chitosan modified with NBT is depicted in Figure 3. The infrared spectra of CS/NBT, as seen in Figure 3, has a Ti-O stretching vibration peak close to 541 cm^{-1}, which belongs to the NBT characteristic peak [32]. The stretching vibrations of attached groups like N-H and O-H on the Chitosan polymer can be identified by the broadband of the modified chitosan's infrared spectra at 3300 cm^{-1}. The asymmetric stretching vibrations of the C-H group in the chitosan chain are represented by the band at 2864 cm^{-1}, while the symmetric stretching vibrations are represented by the band at 2916 cm^{-1}. These bands, which are hallmarks of polysaccharides, can be seen in various polysaccharide spectra [33,34]. Residual N-acetyl groups were identified through characteristic bands observed at 1650 cm^{-1} (corresponding to the C=O stretching of amide I) and 1317 cm^{-1} (representing the C-N stretching of amide III) [35]. Figure 3 shows also a band near 1562 cm^{-1} which resembles to the N-H bending of the primary amine [36]. All found bands agree rather well with what was discovered by others in previous studies [37,38].

The IR spectra presents some changes as a result of the NBT addition. The spectra clearly show a correlation between the quantity of NBT particles present in the Chitosan matrix and the width of the bands related to the N-H and O-H groups. Additionally, the appearance of the NBT's characteristic peak is evident as the amount of NBT particles increases. This may be a sign that coordination bonds are forming between different groups of chitosan and NBT nanoparticles. As a result, it was determined that NBT particles would be found between chitosan chains that were

Preprints (www.preprints.org) | NOT PEER-REVIEWED | Posted: 12 September 2023 doi:10.20944/preprints202309.0687.v1

connected via functional groups, indicating that NBT had been successfully added onto the surface of chitosan [39].

Furthermore, Spectrum analysis (FT-IR) is used to calculate the chitosan's degree of deacetylation (DDA% = 87.9%), using this formula as suggested in literature [40].

$$DDA\% = 100 - [\,(A_{1650}cm^{-1}/A_{3363}cm^{-1}) * 100/1.33]$$

With: A_{1650} cm^{-1}: Absorbance at 1650 cm^{-1} of Amide I, A_{3363} cm^{-1}: Absorbance at 3363 cm^{-1} of the hydroxyl band and 1.33 is a correction factor used to normalize absorbance values.

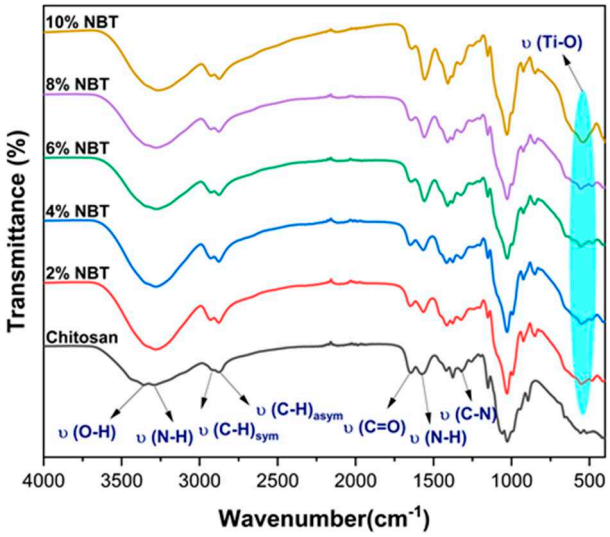

Figure 3. FT-IR spectra of nanocomposite chitosan/NBT.

Figure 4 shows the ambient temperature of Raman spectra of the composite samples CS/NBT. Each of these spectra agrees well with those mentioned in the bibliography [41,42].

The spectra display the aliphatic vibrations νCH, which were attributed to the fingerprint region of chitosan that appears around 2900 cm^{-1} [43,44]. As is widely known, Raman spectroscopy is a sensitive technique for detecting structural changes and for investigating how phonon modes change with temperature, pressure, etc. As previously stated, NBT crystallize in the rhombohedral R3c phase, and this phase persists until approximately 200 °C [45]. The sodium bismuth titanate (NBT) Raman response is shown to be similar with earlier results [46,47]. Note that the provided Raman spectra demonstrate the presence of a low frequency mode at a wavelength of about 70 cm^{-1}. Despite its obvious significance, many studies that examined NBT Raman spectra did not take this last frequency component into account. However, certain authors [48,49] had a particular interest in this specific region. For example, Siny et al. examined the low frequency mode's behavior in order to emphasize the presence of a central component in NBT single crystals that is well-known in relaxor ferroelectrics [49].

Other research on ceramic systems [50] and NBT-xBT single crystal have examined the temperature variation in the Raman spectra of the low frequency mode for studying the $BaTiO_3$ doping effect in NBT system. As shown in Figure 4, the Raman spectrum of NBT consists of three Raman regions: two distinctive bands with frequency mode around 70 cm^{-1} and 150 cm^{-1} that belong to the vibrations of Bi-O and Na-O, respectively, which define the region 1. Furthermore, the intense vibrational Raman mode around 240 cm^{-1} that mostly involves B-site cations, thus Ti-O vibrations, which revealed to be the main feature in our spectra [46]. According to Maria et al. [51], the last region modes between 400 cm^{-1} and 700 cm^{-1} are BO_6 tilting modes, which means they are a consequence of TiO_6 octahedral vibrations. These modes, which include oxygen atom variations in perovskites while cations are essentially at rest, are widely known [52].

Preprints (www.preprints.org) | NOT PEER-REVIEWED | Posted: 12 September 2023 doi:10.20944/preprints202309.0687.v1

In the current investigation, there is no discernible frequency variation when NBT is added to the CS polymer. However, it was found that as NBT concentrations increase, the intensity ratio of NBT modes also increases.

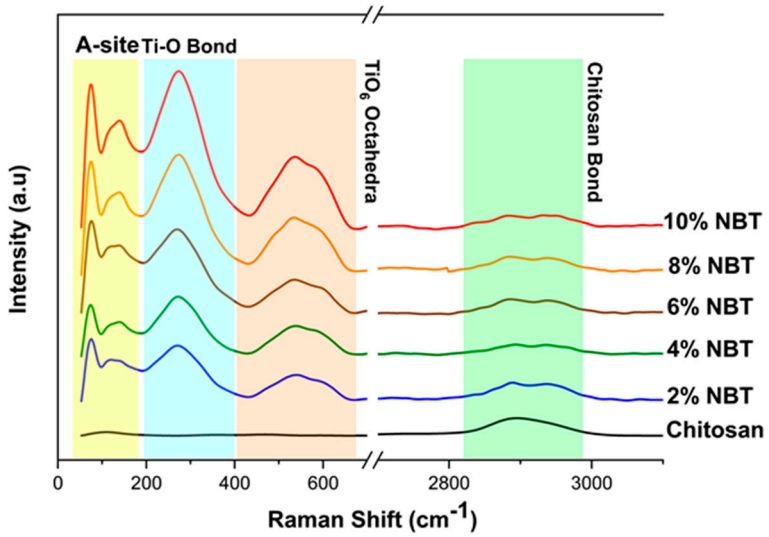

Figure 4. Raman of nanocomposite chitosan/NBT.

3.3. Microstructural analysis

We carried out SEM studies on a variety of CS/NBT composites with various doping concentrations, as shown in Figure 5, in order to more clearly see the distribution of NBT nanoparticles in the CS matrix. Two zones can be seen in Figure 5, the first one is dark and the other is light. Indeed, the light particles are the nanoparticles, while the black region is the CS matrix. On the other hand, Figure 5 illustrates how the NBT nanoparticles are arbitrarily overlaid and interlocked with other particles to form linked grains with a lot of interspaces. The pure CS film also demonstrates the absence of pores and cracks, as previously described in the literature [53,54]. Which shows that the solution casting technique used can successfully disperse the NBT filler in the CS matrix. The packing of the particles became denser as the NBT content increased, demonstrating the remarkable interaction between the CS polymer and NBT particles.

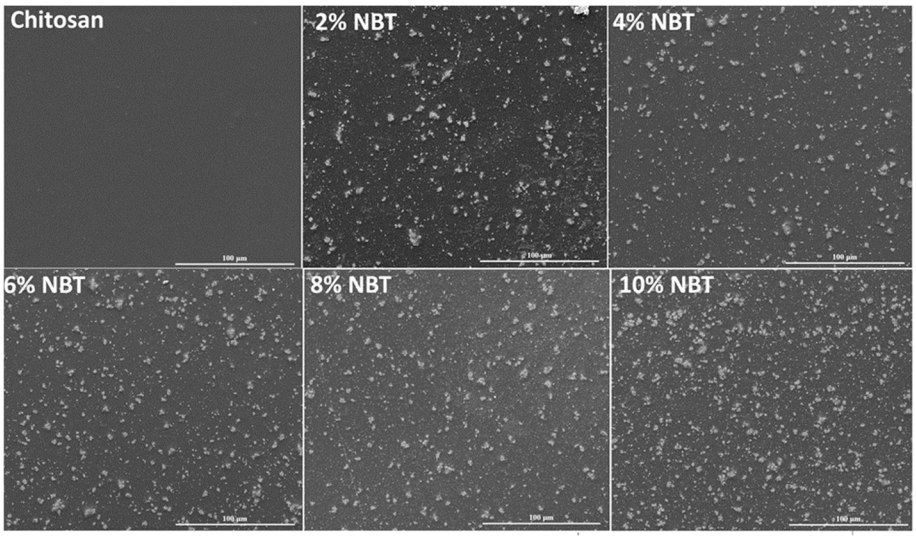

Figure 5. SEM images of nanocomposite chitosan/NBT.

Preprints (www.preprints.org) | NOT PEER-REVIEWED | Posted: 12 September 2023 doi:10.20944/preprints202309.0687.v1

3.4. Dielectric studies

The potential of Chitosan nanocomposite films in terms of their dielectric property remains largely untapped. The dielectric property of CS composite materials possesses great technological promise due to its biocompatibility, cost-effectiveness, and processability. These materials have the potential for various applications in next-generation actuators, fuel cells, sensors, self-regulating heaters, and capacitors. Moreover, by tuning the dielectric property of flexible and biocompatible films, they could serve as artificial muscles for future medical treatments and play a significant role in the development of "smart skins" in the medical field [55–57]. Limited research has been conducted on the dielectric properties of specific synthetic polymer composites [58].

Figure 6 illustrates the measured dielectric constants of the Chitosan composite films at room temperature, as a function of the NBT content, across a frequency range spanning from 100 Hz to 10^6 Hz. All the composite films displayed higher dielectric values when compared to the pure Chitosan film (as illustrated in Figure 6). The increase in the quantity of NBT particles resulted in an elevation of dielectric values due to the corresponding increase in space polarization within the interface of the composite materials. It is a commonly observed trend for dielectric substances to exhibit a gradual decrease in their dielectric constant as the frequency of the electric field rises. This phenomenon is attributed to the inability of the polarization mechanism to keep up with the rapid changes in the electric field at higher frequencies which could be attributed to the effect of the electrode contacts. Consequently, the contribution of polarization to the overall dielectric constant diminishes at high frequency due to dielectric relaxation [23]. Thus, the dielectric permittivity values of the samples should be taken at low frequency for comparison.

For the NBT powder fractions of 2%, 4%, 6%, 8%, and 10%, the dielectric constant values showed an increase compared to the dielectric constant of the pure polymer, starting from 22 and rising to 26, 29, 43, 46, and 82 respectively, at 100 Hz. This increase in relative permittivity can be attributed to two main factors: firstly, it is due to the higher concentration of NBT powder in the composite. When subjected to an external electric field, a significant accumulation of charge occurs, leading to polarization at the interface between the particles and the matrix. This accumulation of charge and subsequent polarization contribute to the overall increase in the dielectric constant [32]. Secondly, the inherent dielectric constant of the NBT powder itself is approximately 600, which is considerably higher than that of the CS polymer. This significant disparity in dielectric constants between the NBT powder and the CS polymer further contributes to the overall increase in the dielectric constant of the CS/NBT composite with increasing filler doping concentration.

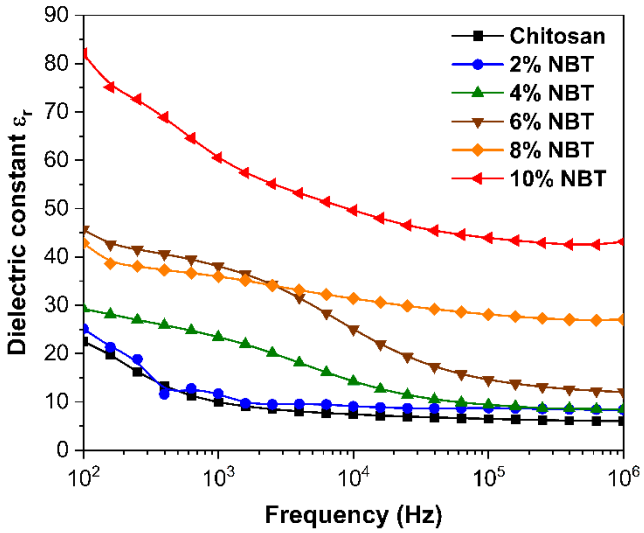

Figure 6. Variation of dielectric constant of chitosan/NBT films with frequency.

Preprints (www.preprints.org) | NOT PEER-REVIEWED | Posted: 12 September 2023 doi:10.20944/preprints202309.0687.v1

3.5. Local Piezoelectric Responses

The surface morphology and piezoelectric response of the CS/NBT10% NCs were investigated at the nanoscale by TM-AFM and PFM, respectively. The typical AFM topography recorded over a large region (50×50 μm²) is shown in Figure 7a, where a relatively even distribution and variable grain size of NBT particles in the CS/NBT10% thin film is observed. Such a rough surface is in agreement with the hybrid polymer/ceramic nature of the sample. Figure 7b presents a zoom-in image of the yellow circled area on the previous image. It clearly shows a rectangular object of nanometric size, which can be thoroughly attributed to an NBT particle.

Figure 7c and d exhibit the as-grow PFM amplitude and phase signals acquired over the region presented in Figure 7b. The contrasts observed in both amplitude and phase images strongly suggest the presence of piezoelectric and ferroelectric activity associated to a well-defined domain structure within the CS/NBT10% film. In addition, this activity is confined to the area previously assigned to the nanoparticle, while no piezoresponse seems to be detected beyond this region. These results reveal the expected distribution of polarized ferroelectric domains into the NBT particles, and suggest the polymer matrix has no electroactive properties. Due to the elaboration method of the composite films, we cannot exclude the presence of a superficial polymer layer covering the ceramic particles. Although this thin Chitosan layer over the surface of the nanofillers reduces the quality of the surface morphology recorded by TM-AFM, it does not prevent the detection of local spontaneous piezo-activity when using PFM technique. Such result was previously reported in PVDF/$BaTiO_3$ composite films [25], and explained by the very high electric field produced beneath the tip combined with the DART-PFM method which amplifies the electromechanical response.

To better assess the piezoelectric behavior of the NBT particles as well as the Chitosan matrix, we further probed the region depicted in the image of Figure 7b-d using the spectroscopic mode of PFM. More specifically, four specific locations were investigated, numbered from 1 to 4 on Figure 7c. The characteristic measured piezoloops at each location are shown in Figure 7e-h. First, when probing areas corresponding to the previously identified NBT particle (points 1 to 3 in Figure 7c), well-defined amplitude and phase (simultaneously recorded) remnant PFM loops are obtained. Indeed, clear hysteresis associated to the 180° phase difference signifying two constant states with opposite polarity for phase loops, and butterfly-shaped signal for amplitude loops are observed, which are both the signature of nanoscale ferro- and piezoelectricity. In addition, such phase PFM responses provide evidence of the efficiency of domain polarization reversal into the NBT particles. On the other hand, no piezoresponse is detected when probing the regions surrounding the particle and associated with the polymer matrix, as observed in Figure 7h (point 4). These results corroborate the as-grown PFM activity observed by scanning the CS/NBT10% film surface (Figure 7c and d), and clearly confirm the electromechanical behavior of the NBT inclusions and the non-polar nature of the Chitosan matrix. In addition, the low coercive voltage determined from the phase loops (about 3.9 V) is in full agreement with the inorganic nature of the probed compound, where the crystalline structure is more homogeneous compared to organic ones. Now, by carefully examining the point 3, we observe that the probed area is slightly outside of the particle. Given that the matrix is non-piezoelectric, the detected response is attributed to the particle, which is buried deeper beneath the polymer layer. It is further supported by the lower PFM amplitude detected on the corresponding loop compared to the two other piezoloops presented in Figure 7e and f. This result further demonstrates the high sensitivity of the PFM tool for probing the electromechanical behavior of nanoparticles dispersed within a low-permittivity polymer matrix.

Preprints (www.preprints.org) | NOT PEER-REVIEWED | Posted: 12 September 2023 doi:10.20944/preprints202309.0687.v1

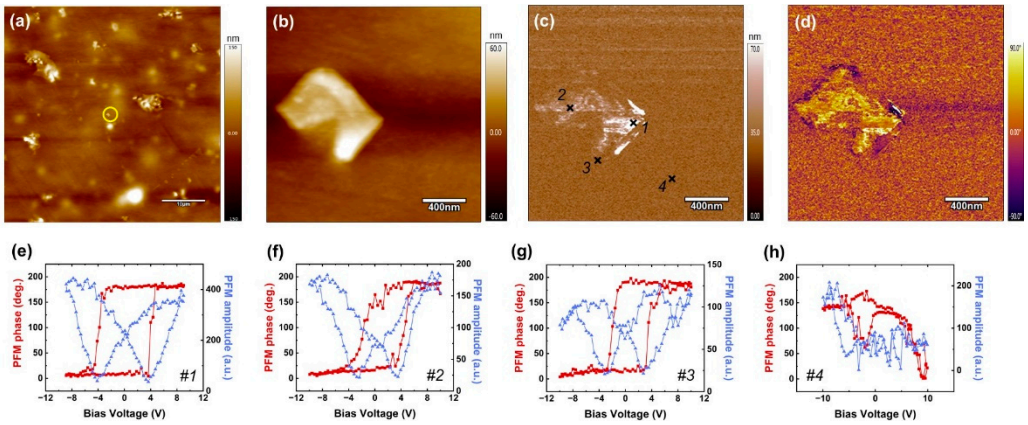

Figure 7. (a, b) AFM topographies, and PFM (c) amplitude and (d) phase images recorded on the CS/NBT10% film. (e-h) Remnant phase and amplitude piezoloops measured in points 1 to 4 in (c).

3.6. Optical investigations

Figure 8a and 8b show the total transmittance (T) and reflectance spectrum (R) respectively for different samples. The Chitosan sample exhibits the typical behaviour which is expected for this material with a thickness of around 30 µm. The refractive index is slightly above 1.5 between 800 nm and 400 nm and the absorption coefficient strongly increases below 250 nm. This is consistent with literature data [59].

The spectra of the composites exhibit a sharp drop around 370 nm which corresponds to signature of the NBT band gap described in literature [60]. However, one also observes another outcome related to the introduction of NBT in the Chitosan matrix which is surprising. In fact, even at low NBT concentrations a strong drop of the transmittance and a high increase of the reflectance occurs in the 400-800 nm range compared with the pure Chitosan sample. For instance, the reflectance of the 2% NBT composite increases from about 7% to more than 25%.

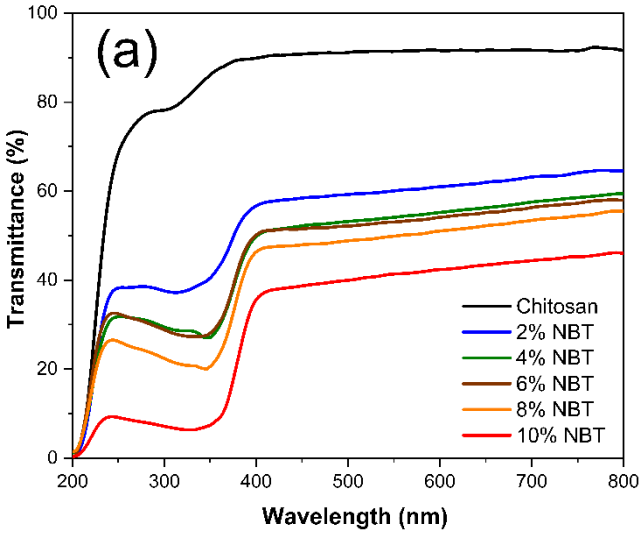

Preprints (www.preprints.org) | NOT PEER-REVIEWED | Posted: 12 September 2023 doi:10.20944/preprints202309.0687.v1

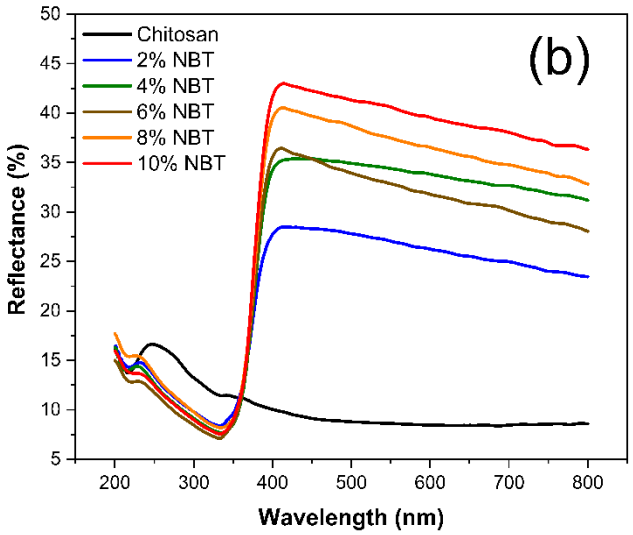

Figure 8. Optical response of pure Chitosan and nanocomposites a): transmittance b) reflectance.

It is well known that the optical properties of composites, displaying non-uniformity at a scale much smaller than the light wavelength., can often be described by an effective dielectric constant framework of effective medium approximations (EMA) [61]. However, for our composites this approach failed. The observed behaviour of the spectra cannot be described by usual mixtures of the dielectric functions of the two phases. It turned out impossible to fit the composite spectra using the main effective medium models (Bruggeman, Maxwell Garnett, Looyenga) [61] or even a more general EMA approach like the Bergman representation [62].

The shapes of the experimental reflectance spectra, with a continuous increase of R with energy in the 400-800 nm range, actually suggest a scattering mechanism. In order to explore this idea, we modelized the spectra with a Mie theory approach using the commercial spectral ray-tracing simulations software SPRAY [63]. In this model the nanocomposite is described by a matrix composed of Chitosan and embedded NBT particles as spheric Mie scatterer. Moreover, an air-composite interface was introduced in order to better simulate the experimental conditions of the reflectance measurement of the samples. The only adjustable fit parameters were the size distribution and the volume fraction of the NBT particles. For the NBT the dielectric function in the range of 300-800 nm was taken from ref. [60] as it matched well the observed reflectance spectra of our pure NBT powders and for the Chitosan matrix the dielectric function extracted from the R and T spectra of the pure Chitosan sample were taken.

The simulation consisted of tracing the rays of 15000 photons impacting the composite surface for each wavelength with a maximum of 10000 possible scattering events per photon in order to modelize the scattering and absorption behaviour of the composite. The scattering and absorbing medium is characterized by the following quantities: S = scattering probability/distance and K = absorption probability/distance. Figure 9a exhibits the respective reflectance curves of the 2% 6% and 10% samples and in figure 9b the corresponding K and S curves are shown. The slight fluctuations of the fit curves could be smoothed by using a much higher number of photons but this makes calculations very time consuming without improving the main outcome.

Preprints (www.preprints.org) | NOT PEER-REVIEWED | Posted: 12 September 2023 doi:10.20944/preprints202309.0687.v1

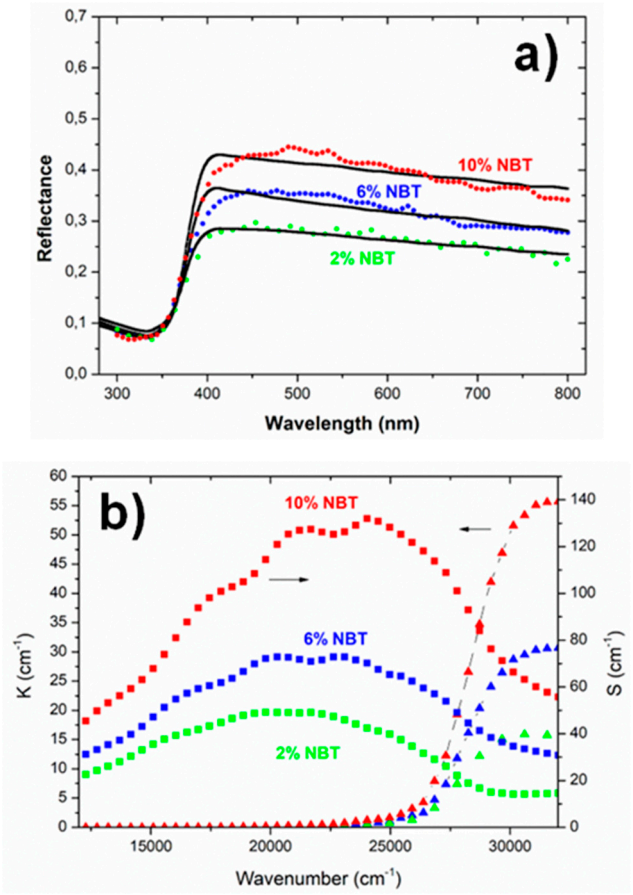

Figure 9. NBT as Mie scattering particles embedded in the Chitosan matrix. a) examples of fits for 2%,6% and 10% NBT: solid lines are experimental spectra and dotted curves are modelized spectra using Mie scattering approach. b) corresponding Mie scattering values K (▲) and S (■).

As illustrated in Figure 9a the Mie model can fairly reproduce the optical response in the 450-800 nm range with a very limit number of fit parameters. It turns out that only particles with diameter sizes between 100 nm and 400 nm significantly contribute to the scattering behaviour. This explains why the determined volume fraction of the scattering particles in the model is quite low: between 0.1% (2% NBT) and 0.4%. (10% NBT) Bigger particles or even clusters as revealed by SEM (Figure 5) might only slightly contribute to the higher reflectance by an effective medium mixture of the two phases. The spectral region around 370-400 nm is dominated by the NBT bandgap and is illustrated by the sharp increase of K in Figure 9b. Note that 27000 cm^{-1} corresponds to 370 nm. However, a more detailed study of the simulation reveals that small particles with 100 to 150 nm size also contribute to the shape of the absorption edge around 400 nm. Increasing the weight of these particles in the distribution at the cost of those of 200-400 nm size leads to a bitter fit of the edge but deteriorates the fit in the red region of the spectra (above 600 nm). The examples shown in Figure 9a are the result of the best compromise in the size distribution.

4. Conclusions

In summary, the successful fabrication of flexible composite films combining polymer and ceramic has been achieved by incorporating sodium bismuth titanate (NBT), a lead-free piezoelectric material, into a Chitosan (CS) polymer matrix derived from the shells of Parapenaeus longirostris shrimp. These films were synthesized with varying amounts of NBT filler and subjected to thorough investigations. The produced Chitosan membrane and the nanocomposite chitosan/NBT membrane were characterized by diverse techniques. X-ray diffraction (XRD) analyses validated the presence of characteristic peaks corresponding to both chitosan and NBT, which exhibited pure perovskite phase with the R3c space group. The Fourier-transform infrared (FT-IR) spectra of CS/NBT films indicated

an increasing prominence of NBT's distinctive peak with higher NBT particle concentrations, potentially indicating the formation of coordination bonds between different chitosan groups and NBT nanoparticles. Scanning electron microscopy (SEM) images depicted two discernible regions: a dark region representing the CS matrix and a lighter area signifying the NBT nanoparticle presence. These nanoparticles were observed to arrange arbitrarily, interlocking with other particles to create interconnected grains interspersed with ample gaps. The optical behavior above 400 nm is largely dominated by light scattering of NBT nanoparticles within the diameter range of 100-400 nm while the NBT bandgap introduces a sharp edge around 370 nm. Incorporating NBT particles into the polymer matrix notably enhanced the dielectric permittivity, surpassing values reported in previous studies. The thorough structural analysis of the films highlighted the significant interaction between the CS polymer and NBT particles. Additionally, nanoscale piezoelectric measurements conducted on the CS/NBT10% film showcased an electromechanical behavior. This promising result paves the way for potential applications of such CS-based composites in actuator, sensor, or energy harvesting systems.

Author Contributions: Jacem Zidani: samples preparation, investigation, writing—original draft; Khaoula Hassine: samples preparation, investigation; Moneim Zannen: visualization, Writing - Review & Editing, validation. Andreas Zeinert: formal analysis, writing—original draft, validation. Antonio Da Costa: Investigation, data curation. Anthony Ferri: Investigation, Writing - Review & Editing. Mustapha Majdoub: validation, supervision. Jamal Belhadi: Investigation, Writing - Review & Editing. Mimoun El Marssi: visualization, validation. Abdelilah Lahmar: Conceptualization, Writing - Review & Editing, visualization, validation, supervision.

Data Availability Statement: Not applicable.

Acknowledgments: This work was supported by the projects: PHC UTIQUE 2022, Grant N° 47593XH and by NAP project in the framework of CPER Manifest 2021-2027.

Conflicts of Interest: The authors declare no conflict of interest.

References

1. S. Mondal, T. Paul, S. Maiti, B.K. Das, K.K. Chattopadhyay, Human motion interactive mechanical energy harvester based on all inorganic perovskite-PVDF, Nano Energy. 74 (2020) 104870. https://doi.org/10.1016/j.nanoen.2020.104870.
2. B. Dudem, D.H. Kim, L.K. Bharat, J.S. Yu, Highly-flexible piezoelectric nanogenerators with silver nanowires and barium titanate embedded composite films for mechanical energy harvesting, Appl. Energy. 230 (2018) 865–874. https://doi.org/10.1016/j.apenergy.2018.09.009.
3. J. Jacob, N. More, K. Kalia, G. Kapusetti, Piezoelectric smart biomaterials for bone and cartilage tissue engineering, Inflamm. Regen. 38 (2018) 2. https://doi.org/10.1186/s41232-018-0059-8.
4. A.T. Hazmi, F.B. Ahmad, M.H. Maziati Akmal, A.A. Md Ralib, F. Binti Ali, Fungal chitosan for potential application in piezoelectric energy harvesting: Review on experimental procedure of chitosan extraction, Alex. Eng. J. 67 (2023) 105–116. https://doi.org/10.1016/j.aej.2022.08.020.
5. H. Kaczmarek, B. Królikowski, E. Klimiec, M. Chylińska, D. Bajer, Advances in the study of piezoelectric polymers, Russ. Chem. Rev. 88 (2019) 749–774. https://doi.org/10.1070/RCR4860.
6. Y. Lu, J. Chen, Z. Cheng, S. Zhang, The PZT/Ni unimorph magnetoelectric energy harvester for wireless sensing applications, Energy Convers. Manag. 200 (2019) 112084. https://doi.org/10.1016/j.enconman.2019.112084.
7. S.H. Wankhade, S. Tiwari, A. Gaur, P. Maiti, PVDF–PZT nanohybrid based nanogenerator for energy harvesting applications, Energy Rep. 6 (2020) 358–364. https://doi.org/10.1016/j.egyr.2020.02.003.
8. B. Hilczer, J. Kułek, E. Markiewicz, M. Kosec, B. Malič, Dielectric relaxation in ferroelectric PZT–PVDF nanocomposites, J. Non-Cryst. Solids. 305 (2002) 167–173. https://doi.org/10.1016/S0022-3093(02)01103-1.
9. J. Rödel, K.G. Webber, R. Dittmer, W. Jo, M. Kimura, D. Damjanovic, Transferring lead-free piezoelectric ceramics into application, J. Eur. Ceram. Soc. 35 (2015) 1659–1681. https://doi.org/10.1016/j.jeurceramsoc.2014.12.013.

10. M.H.M. Akmal, F.B. Ahmad, Bionanomaterial Thin Film for Piezoelectric Applications, in: A.T. Jameel, A.Z. Yaser (Eds.), Adv. Nanotechnol. Its Appl., Springer Singapore, Singapore, 2020: pp. 63–82. https://doi.org/10.1007/978-981-15-4742-3_4.
11. S.K. Ghosh, D. Mandal, Bio-assembled, piezoelectric prawn shell made self-powered wearable sensor for non-invasive physiological signal monitoring, Appl. Phys. Lett. 110 (2017) 123701. https://doi.org/10.1063/1.4979081.
12. J.L. Chen, Y. Zhao, Effect of Molecular Weight, Acid, and Plasticizer on the Physicochemical and Antibacterial Properties of β-Chitosan Based Films, J. Food Sci. 77 (2012) E127–E136. https://doi.org/10.1111/j.1750-3841.2012.02686.x.
13. K. Kim, M. Ha, B. Choi, S.H. Joo, H.S. Kang, J.H. Park, B. Gu, C. Park, C. Park, J. Kim, S.K. Kwak, H. Ko, J. Jin, S.J. Kang, Biodegradable, electro-active chitin nanofiber films for flexible piezoelectric transducers, Nano Energy. 48 (2018) 275–283. https://doi.org/10.1016/j.nanoen.2018.03.056.
14. M.I. Zamli, F.B. Ahmad, M.H.M. Akmal, Extraction of microbial chitosan for piezoelectric application, IOP Conf. Ser. Mater. Sci. Eng. 1045 (2021) 012037. https://doi.org/10.1088/1757-899X/1045/1/012037.
15. A. Hänninen, S. Rajala, T. Salpavaara, M. Kellomäki, S. Tuukkanen, Piezoelectric Sensitivity of a Layered Film of Chitosan and Cellulose Nanocrystals, Procedia Eng. 168 (2016) 1176–1179. https://doi.org/10.1016/j.proeng.2016.11.397.
16. E. Praveen, S. Murugan, K. Jayakumar, Investigations on the existence of piezoelectric property of a bio-polymer – chitosan and its application in vibration sensors, RSC Adv. 7 (2017) 35490–35495. https://doi.org/10.1039/C7RA04752E.
17. A. Safari, V.F. Janas, Processing of fine-scale piezoelectric ceramic/polymer composites for transducer applications, Ferroelectrics. 196 (1997) 187–190. https://doi.org/10.1080/00150199708224159.
18. M. Maksimovic, The Role of Green Internet of Things (G-IoT) and Big Data in Making Cities Smarter, Safer and More Sustainable, Int. J. Comput. Digit. Syst. 6 (2017) 175–184. https://doi.org/10.12785/IJCDS/060403.
19. J. Hafsa, M.A. Smach, B. Charfeddine, K. Limem, H. Majdoub, S. Rouatbi, Antioxidant and antimicrobial proprieties of chitin and chitosan extracted from Parapenaeus Longirostris shrimp shell waste, Ann. Pharm. Fr. 74 (2016) 27–33. https://doi.org/10.1016/j.pharma.2015.07.005.
20. H.K. No, S.P. Meyers, Preparation and Characterization of Chitin and Chitosan—A Review, J. Aquat. Food Prod. Technol. 4 (1995) 27–52. https://doi.org/10.1300/J030v04n02_03.
21. A. Tolaimate, J. Desbrieres, M. Rhazi, A. Alagui, Contribution to the preparation of chitins and chitosans with controlled physico-chemical properties, Polymer. 44 (2003) 7939–7952. https://doi.org/10.1016/j.polymer.2003.10.025.
22. G. Galed, B. Miralles, I. Panos, A. Santiago, A. Heras, -Deacetylation and depolymerization reactions of chitin/chitosan: Influence of the source of chitin, Carbohydr. Polym. 62 (2005) 316–320. https://doi.org/10.1016/j.carbpol.2005.03.019.
23. P. Mujeeb Rahman, V.M. Abdul Mujeeb, K. Muraleedharan, S.K. Thomas, Chitosan/nano ZnO composite films: Enhanced mechanical, antimicrobial and dielectric properties, Arab. J. Chem. 11 (2018) 120–127. https://doi.org/10.1016/j.arabjc.2016.09.008.
24. B.J. Rodriguez, C. Callahan, S.V. Kalinin, R. Proksch, Dual-frequency resonance-tracking atomic force microscopy, Nanotechnology. 18 (2007) 475504. https://doi.org/10.1088/0957-4484/18/47/475504.
25. A. Ferri, S. Barrau, R. Bourez, A. Da Costa, M.-H. Chambrier, A. Marin, J. Defebvin, J.M. Lefebvre, R. Desfeux, Probing the local piezoelectric behavior in stretched barium titanate/poly(vinylidene fluoride) nanocomposites, Compos. Sci. Technol. 186 (2020) 107914. https://doi.org/10.1016/j.compscitech.2019.107914.
26. M. Zannen, A. Lahmar, M. Dietze, H. Khemakhem, A. Kabadou, M. Es-Souni, Structural, optical, and electrical properties of Nd-doped $Na_{0.5}Bi_{0.5}TiO_3$, Mater. Chem. Phys. 134 (2012) 829–833. https://doi.org/10.1016/j.matchemphys.2012.03.076.
27. J.I. Langford, A.J.C. Wilson, Scherrer after sixty years: A survey and some new results in the determination of crystallite size, J. Appl. Crystallogr. 11 (1978) 102–113. https://doi.org/10.1107/S0021889878012844.
28. S. Govindan, E.A.K. Nivethaa, R. Saravanan, V. Narayanan, A. Stephen, Synthesis and characterization of chitosan–silver nanocomposite, Appl. Nanosci. 2 (2012) 299–303. https://doi.org/10.1007/s13204-012-0109-5.
29. A. Pawlak, M. Mucha, Thermogravimetric and FTIR studies of chitosan blends, Thermochim. Acta. 396 (2003) 153–166. https://doi.org/10.1016/S0040-6031(02)00523-3.

30. M. Benyoussef, M. Zannen, J. Belhadi, B. Manoun, J.-L. Dellis, A. Lahmar, M. El Marssi, Complex impedance and Raman spectroscopy of $Na_{0.5}(Bi_{1-x}Dyx)_{0.5}TiO_3$ ceramics, Ceram. Int. 46 (2020) 10979–10991. https://doi.org/10.1016/j.ceramint.2020.01.114.
31. L.-H. Li, J.-C. Deng, H.-R. Deng, Z.-L. Liu, L. Xin, Synthesis and characterization of chitosan/ZnO nanoparticle composite membranes, Carbohydr. Res. 345 (2010) 994–998. https://doi.org/10.1016/j.carres.2010.03.019.
32. Z. Xu, L. Weng, L. Guan, X. Zhang, X. Wang, Z. Wu, Enhanced energy storage performance of PVDF composite films with $Na_{0.5}Bi_{0.5}TiO_3$ particles, J. Mater. Sci. Mater. Electron. 32 (2021) 28129–28143. https://doi.org/10.1007/s10854-021-07191-9.
33. R.F. Melo-Silveira, G.P. Fidelis, M.S.S.P. Costa, C.B.S. Telles, N. Dantas-Santos, S.D.O. Elias, V.B. Ribeiro, A.L. Barth, A.J. Macedo, E.L. Leite, H.A.O. Rocha, In Vitro Antioxidant, Anticoagulant and Antimicrobial Activity and in Inhibition of Cancer Cell Proliferation by Xylan Extracted from Corn Cobs, Int. J. Mol. Sci. 13 (2011) 409–426. https://doi.org/10.3390/ijms13010409.
34. W.F. Wolkers, A.E. Oliver, F. Tablin, J.H. Crowe, A Fourier-transform infrared spectroscopy study of sugar glasses, Carbohydr. Res. 339 (2004) 1077–1085. https://doi.org/10.1016/j.carres.2004.01.016.
35. M. Fernandes Queiroz, K. Melo, D. Sabry, G. Sassaki, H. Rocha, Does the Use of Chitosan Contribute to Oxalate Kidney Stone Formation?, Mar. Drugs. 13 (2014) 141–158. https://doi.org/10.3390/md13010141.
36. S.-H. Lim, S.M. Hudson, Synthesis and antimicrobial activity of a water-soluble chitosan derivative with a fiber-reactive group, Carbohydr. Res. 339 (2004) 313–319. https://doi.org/10.1016/j.carres.2003.10.024.
37. A.B. Vino, P. Ramasamy, V. Shanmugam, A. Shanmugam, Extraction, characterization and in vitro antioxidative potential of chitosan and sulfated chitosan from Cuttlebone of Sepia aculeata Orbigny, 1848, Asian Pac. J. Trop. Biomed. 2 (2012) S334–S341. https://doi.org/10.1016/S2221-1691(12)60184-1.
38. C. Song, H. Yu, M. Zhang, Y. Yang, G. Zhang, Physicochemical properties and antioxidant activity of chitosan from the blowfly Chrysomya megacephala larvae, Int. J. Biol. Macromol. 60 (2013) 347–354. https://doi.org/10.1016/j.ijbiomac.2013.05.039.
39. I. Perelshtein, E. Ruderman, N. Perkas, T. Tzanov, J. Beddow, E. Joyce, T.J. Mason, M. Blanes, K. Mollá, A. Patlolla, A.I. Frenkel, A. Gedanken, Chitosan and chitosan–ZnO-based complex nanoparticles: formation, characterization, and antibacterial activity, J. Mater. Chem. B. 1 (2013) 1968. https://doi.org/10.1039/c3tb00555k.
40. A. Domard, M. Rinaudo, Preparation and characterization of fully deacetylated chitosan, Int. J. Biol. Macromol. 5 (1983) 49–52. https://doi.org/10.1016/0141-8130(83)90078-8.
41. S. Behara, L. Ghatti, S. Kanthamani, M. Dumpala, T. Thomas, Structural, optical, and Raman studies of Gd doped sodium bismuth titanate, Ceram. Int. 44 (2018) 12118–12124. https://doi.org/10.1016/j.ceramint.2018.03.233.
42. A. Zając, J. Hanuza, M. Wandas, L. Dymińska, Determination of N-acetylation degree in chitosan using Raman spectroscopy, Spectrochim. Acta. A. Mol. Biomol. Spectrosc. 134 (2015) 114–120. https://doi.org/10.1016/j.saa.2014.06.071.
43. D. Kim, V. Dhand, K. Rhee, S.-J. Park, Study on the Effect of Silanization and Improvement in the Tensile Behavior of Graphene-Chitosan-Composite, Polymers. 7 (2015) 527–551. https://doi.org/10.3390/polym7030527.
44. M.J. Alvarez-Figueroa, D. Narváez-Araya, N. Armijo-Escalona, E.A. Carrasco-Flores, J.V. González-Aramundiz, Design of Chitosan Nanocapsules with Compritol 888 ATO® for Imiquimod Transdermal Administration. Evaluation of Their Skin Absorption by Raman Microscopy, Pharm. Res. 37 (2020) 195. https://doi.org/10.1007/s11095-020-02925-6.
45. G. Das Adhikary, B. Mahale, B.N. Rao, A. Senyshyn, R. Ranjan, Depoling phenomena in $Na_{0.5}Bi_{0.5}TiO_3$ – $BaTiO_3$: A structural perspective, Phys. Rev. B. 103 (2021) 184106. https://doi.org/10.1103/PhysRevB.103.184106.
46. R. Roukos, N. Zaiter, D. Chaumont, Relaxor behaviour and phase transition of perovskite ferroelectrics-type complex oxides (1–x) $Na_{0.5}Bi_{0.5}TiO_3$–$xCaTiO_3$ system, J. Adv. Ceram. 7 (2018) 124–142. https://doi.org/10.1007/s40145-018-0264-6.
47. K. Thangavelu, S. Asthana, Monoclinic Cc -phase stabilization in magnetically diluted lead free $Na_{1/2}Bi_{1/2}TiO_3$ —Evolution of spin glass like behavior with enhanced ferroelectric and dielectric properties, Mater. Res. Express. 2 (2015) 096301. https://doi.org/10.1088/2053-1591/2/9/096301.

48. G. De La Flor, T. Malcherek, S. Gorfman, B. Mihailova, Structural transformations in (1 − x) $Na_{0.5}Bi_{0.5}TiO_3$ − x $BaTiO_3$ single crystals studied by Raman spectroscopy, Phys. Rev. B. 96 (2017) 214102. https://doi.org/10.1103/PhysRevB.96.214102.
49. I.G. Siny, E. Husson, J.M. Beny, S.G. Lushnikov, E.A. Rogacheva, P.P. Syrnikov, Raman scattering in the relaxor-type ferroelectric $Na_{1/2}Bi_{1/2}TiO_3$, Ferroelectrics. 248 (2000) 57–78. https://doi.org/10.1080/00150190008223669.
50. K. Datta, A. Richter, M. Göbbels, R.B. Neder, B. Mihailova, Atomistic origin of huge response functions at the morphotropic phase boundary of (1 − x) $Na_{0.5}Bi_{0.5}TiO_3$ − x $BaTiO_3$, Phys. Rev. B. 90 (2014) 064112. https://doi.org/10.1103/PhysRevB.90.064112.
51. N.P. Maria Joseph Raj, A. Ks, G. Khandelwal, N.R. Alluri, S.-J. Kim, A lead-free ferroelectric $Bi_{0.5}Na_{0.5}TiO_3$ based flexible, lightweight nanogenerator for motion monitoring applications, Sustain. Energy Fuels. 4 (2020) 5636–5644. https://doi.org/10.1039/D0SE00963F.
52. D. Rout, V. Subramanian, K. Hariharan, V.R.K. Murthy, V. Sivasubramanian, Raman spectroscopic study of $(Pb_{1-x}Ba_x)(Yb_{1/2}Ta_{1/2})O_3$ ceramics, J. Appl. Phys. 98 (2005) 103503. https://doi.org/10.1063/1.2131188.
53. K.D. Khalil, E.I. Ibrahim, F.A. Al-Sagheer, A novel, efficient, and recyclable biocatalyst for Michael addition reactions and its iron(iii) complex as promoter for alkyl oxidation reactions, Catal. Sci. Technol. 6 (2016) 1410–1416. https://doi.org/10.1039/C5CY01034A.
54. K.D. Khalil, S.M. Riyadh, S.M. Gomha, I. Ali, Synthesis, characterization and application of copper oxide chitosan nanocomposite for green regioselective synthesis of [1,2,3]triazoles, Int. J. Biol. Macromol. 130 (2019) 928–937. https://doi.org/10.1016/j.ijbiomac.2019.03.019.
55. C.K. Chiang, R. Popielarz, Polymer Composites with High Dielectric Constant, Ferroelectrics. 275 (2002) 1–9. https://doi.org/10.1080/00150190214285.
56. S. B. Kondawar, A. D. Dahegaonkar, V. A. Tabhane, D. V. Nandanwar, Thermal And Frequency Dependance Dielectric Properties Of Conducting Polymer/ Fly Ash Composites, Adv. Mater. Lett. 5 (2014) 360–365. https://doi.org/10.5185/amlett.2014.amwc.1036.
57. P.I. Devi, K. Ramachandran, Dielectric studies on hybridised PVDF–ZnO nanocomposites, J. Exp. Nanosci. 6 (2011) 281–293. https://doi.org/10.1080/17458080.2010.497947.
58. A. Qureshi, A. Mergen, M.S. Eroğlu, N.L. Singh, A. Güllüoğlu, Dielectric Properties of Polymer Composites Filled with Different Metals, J. Macromol. Sci. Part A. 45 (2008) 462–469. https://doi.org/10.1080/10601320801977756.
59. D.E. Azofeifa, H.J. Arguedas, W.E. Vargas, Optical properties of chitin and chitosan biopolymers with application to structural color analysis, Opt. Mater. 35 (2012) 175–183. https://doi.org/10.1016/j.optmat.2012.07.024.
60. M. Bousquet, J.-R. Duclère, E. Orhan, A. Boulle, C. Bachelet, C. Champeaux, Optical properties of an epitaxial $Na_{0.5}Bi_{0.5}TiO_3$ thin film grown by laser ablation: Experimental approach and density functional theory calculations, J. Appl. Phys. 107 (2010) 104107. https://doi.org/10.1063/1.3400095.
61. M. Evenschor, P. Grosse, W. Theiss, Optics of two-phase composites, Vib. Spectrosc. 1 (1990) 173–177. https://doi.org/10.1016/0924-2031(90)80032-Y.
62. W. Theiß, The use of effective medium theories in optical spectroscopy, in: R. Helbig (Ed.), Adv. Solid State Phys. 33, Springer Berlin Heidelberg, Berlin, Heidelberg, 1993: pp. 149–176. https://doi.org/10.1007/BFb0107886.
63. WTheiss Hardware and Software, (n.d.). https://www.wtheiss.com/.